

http://pubs.acs.org/journal/aelccp

# Distinct Oxygen Redox Activities in Li<sub>2</sub>MO<sub>3</sub> (M = Mn, Ru, Ir)

Zengqing Zhuo, Kehua Dai, Jinpeng Wu, Liang Zhang, Nobumichi Tamura, Yi-de Chuang, Jun Feng, Jinghua Guo, Zhi-xun Shen, Gao Liu,\* Feng Pan,\* and Wanli Yang\*



Cite This: ACS Energy Lett. 2021, 6, 3417-3424



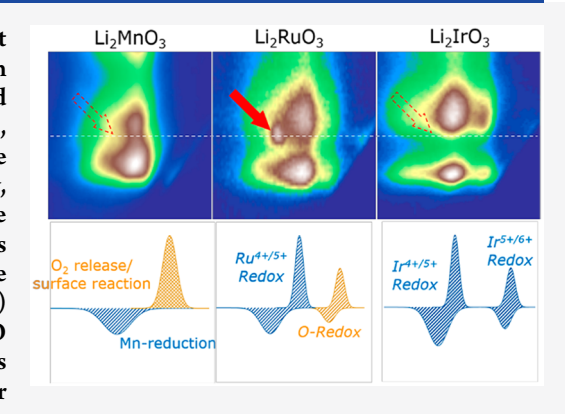
ACCESS

III Metrics & More

Article Recommendations

Supporting Information

ABSTRACT: Li<sub>2</sub>MO<sub>3</sub> (M = transition metal) systems are parent compounds of Li-rich materials and widely considered to offer oxygen redox for high-energy batteries. However, recent clarifications have revealed that, among the three representative Li<sub>2</sub>MO<sub>3</sub> (M = Mn, Ru, Ir) compounds, no reversible oxygen redox takes place in the Mn and Ir systems. Here, we reevaluate the redox reactions in Li<sub>2</sub>RuO<sub>3</sub> through advanced spectroscopy, which shows both Ru redox and highly reversible O redox (96% initial-cycle reversibility, 80% retained after 10 cycles, and 77% after 50 cycles). This is in sharp contrast with the Li<sub>2</sub>MnO<sub>3</sub> and Li<sub>2</sub>IrO<sub>3</sub> systems and concludes the three distinct oxygen behaviors in the Li<sub>2</sub>MO<sub>3</sub> systems during charging: (i) only irreversible oxygen oxidation in Li<sub>2</sub>MnO<sub>3</sub>; (ii) reversible Ru and O redox in Li<sub>2</sub>RuO<sub>3</sub>; (iii) only cationic redox in Li<sub>2</sub>IrO<sub>3</sub>. This work suggests the critical role of transition metals and their coupling to oxygen for maintaining reversible oxygen redox activities for high-energy batteries.



The development of high-energy-density lithium ion batteries (LIBs) has become essential to address today's energy and environmental challenges. As the bottleneck of battery energy density, transition metal (TM) oxide based cathodes have aroused great interest and tremendous efforts on both the fundamental understanding and practical optimizations.<sup>2</sup> The amount of lithium ions in oxide cathodes that is available for electrochemical cycling defines the cycling capacity. Therefore, Li-rich layer oxides with an excessive amount of Li > 1, could potentially offer a higher energy density over conventional compounds. A number of studies of Li-rich cathodes have shown that high capacities could indeed be achieved, which are mostly due to the O anionic redox reaction (ARR) beyond the conventional TM redox activities.<sup>3-9</sup> However, it was also found that the oxygen redox reactions in the Li-rich system, especially the oxygen oxidation reaction during the initial charging, almost inherently triggers irreversible oxygen release and/or surface reactions, which remains a formidable challenge and leads to the notorious hysteresis, voltage fade, and capacity decay.<sup>3-5</sup> In the meantime, several recent clarifications have suggested that some of these detrimental effects are not necessarily from the reversible ARR. 10-12 Therefore, it is critical to distinguish the lattice ARR from other oxygen activities through reliable techniques and perform comparative studies of representative Li-rich systems with different oxygen activities.

Three materials emerge in the families of the layered compounds that represent the most typical Li-rich configurations, Li<sub>2</sub>MnO<sub>3</sub>, Li<sub>2</sub>RuO<sub>3</sub>, and Li<sub>2</sub>IrO<sub>3</sub>. They represent Lirich systems based on 3d, 4d, and 5d TMs with different cationic d levels and hybridization effects that are important for ARR behaviors.<sup>4,13</sup> Other than some detailed structural differences that have been reported before,<sup>8,14–22</sup> all these three materials are layered compounds with a significant amount of Li occupying about 1/3 of the TM sites forming a honeycomb structure, i.e., the typical Li-rich configuration. In the early stage of the study of ARR, all three systems were considered systems with reversible lattice ARR, mostly based on O-K X-ray absorption spectroscopy (XAS) and X-ray photoelectron spectroscopy (XPS) studies.<sup>8,13,15,23-26</sup> However, these conclusions have later been challenged due to the technical reliability issues of the entangled O-K XAS signals with significant TM characters and the shallow probe depths of both soft and hard XPS.<sup>27,28</sup> Indeed, advances in O-K spectroscopy based on high-efficiency mapping of resonant inelastic X-ray scattering (mRIXS), 29,30 together with differ-

Received: May 29, 2021 Accepted: August 31, 2021 Published: September 3, 2021





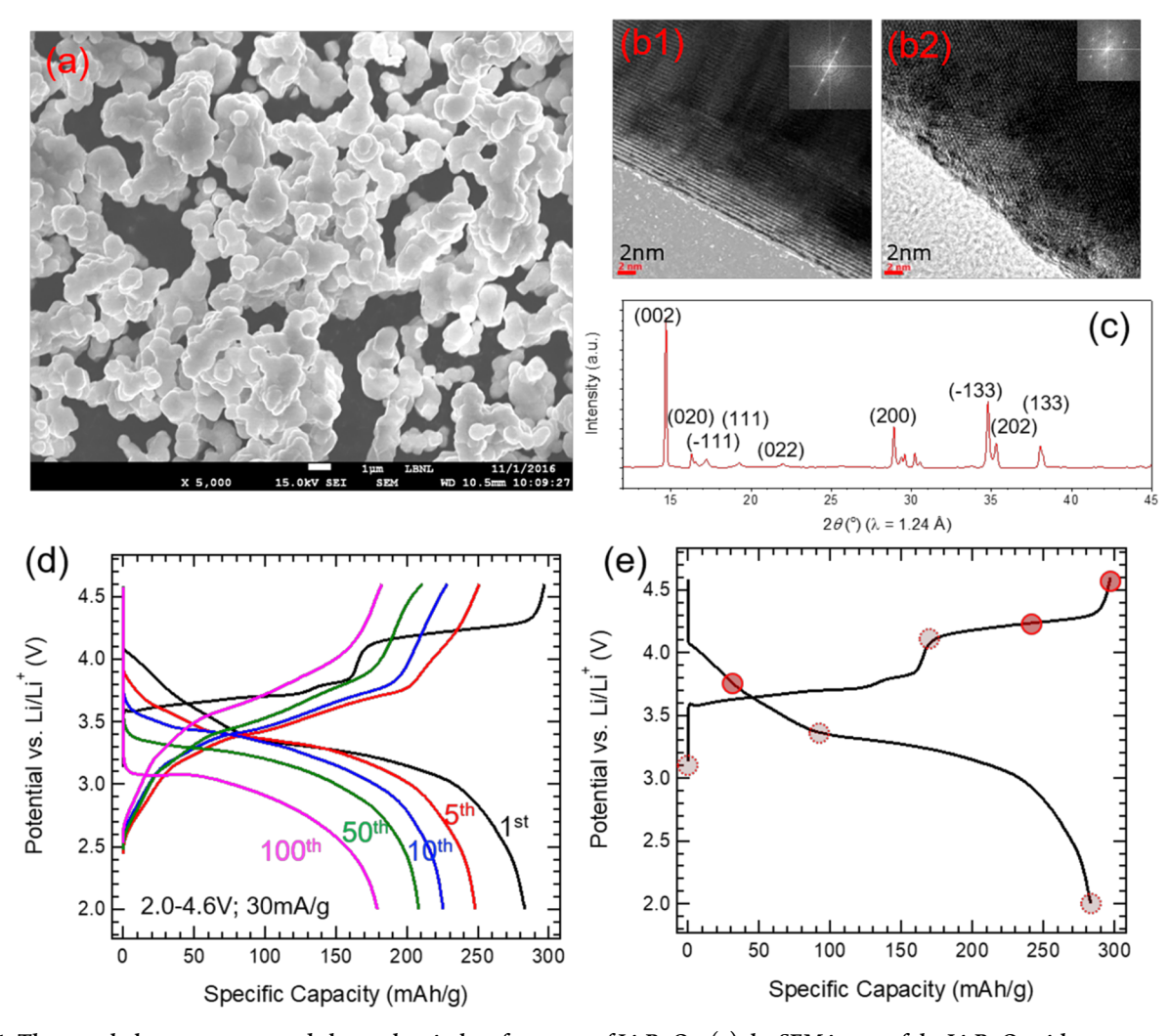


Figure 1. The morphology, structure, and electrochemical performance of  $\text{Li}_2\text{RuO}_3$ : (a) the SEM image of the  $\text{Li}_2\text{RuO}_3$  with mean particle size around 1.3  $\mu\text{m}$ . (b) the HR-TEM image of the  $\text{Li}_2\text{RuO}_3$  viewed along the a (b1) and c (b2) directions; (c) the synchrotron XRD pattern of the  $\text{Li}_2\text{RuO}_3$  with space group C2/c; (d) the selected charge—discharge curves of  $\text{Li}_2\text{RuO}_3$  electrochemically cycled between 2.0 and 4.6 V with current 30 mA/g; (e) the initial cycle curve of the  $\text{Li}_2\text{RuO}_3$  marked by red dots which are characterized through Ru-L and O-K spectroscopy in the following figures.

ential electrochemical mass spectroscopy (DEMS), have clarified that no lattice ARR is involved in the cycling of  $\text{Li}_2\text{MnO}_3$  and  $\text{Li}_2\text{IrO}_3$ .  $^{14,31,32}$  Recent experimental results conclusively show that oxygen oxidation during the initial charging of  $\text{Li}_2\text{MnO}_3$  is only in the form of irreversible oxygen release and surface reactions,  $^{31,32}$  consistent with some earlier theoretical analysis,  $^4$  and fully charged  $\text{Li}_2\text{IrO}_3$  displays only multivalent Ir redox reactions.  $^{14}$  Therefore, interesting questions arise on the redox mechanism of  $\text{Li}_2\text{RuO}_3$ : Is  $\text{Li}_2\text{RuO}_3$  the (only) ARR system among these Li-rich parent compounds? If yes, how reversible and cyclable the ARR is  $\text{Li}_2\text{RuO}_3$ ? What has led to its distinct oxygen activities compared with the Mn and Ir systems?

Herein, we report experimental characterizations of both Ru and O states of  $\rm Li_2RuO_3$  at representative charge and discharge states during the initial, 10th, and 50th cycles. There have been several reports on the redox mechanism of  $\rm Li_2RuO_3$  based on conventional spectroscopy during the early cycles.  $^{13,15,25,26}$  However, as discussed above, clarifications on oxygen activities through reliable techniques are critical to avoid the confusions as in the Mn and Ir systems. Furthermore, the reversibility and cyclability of the ARR in  $\rm Li_2RuO_3$  has not been explored, which

require studies of electrodes after extended cycles and the mRIXS technique that could quantify these important ARR values.<sup>33</sup> Our results of Ru-L XAS and O-K mRIXS consistently show the charge compensation mechanism of Li<sub>2</sub>RuO<sub>3</sub> at different voltage ranges. Lattice ARR is involved at high voltage during initial charging but is extended to much lower energy during discharge, with Ru displaying different bulk and surface behaviors. We further quantified the reversibility of the ARR during the initial cycle, and the retention rate of ARR after the 10th and 50th cycles. Our work confirms and provides the first quantitative evaluation of the ARR in Li<sub>2</sub>RuO<sub>3</sub>, which triggers interesting comparisons among the three Li-rich parent compounds,  $Li_2MO_3$  (M = Mn, Ru, Ir). We discuss the fundamental differences between these three systems based on their distinct mRIXS findings for new insights on critical factors for maintaining reversible ARR in cathode materials.

The structure analysis and electrochemical performance of  $\text{Li}_2\text{RuO}_3$  are shown in Figure 1, which are consistent with the previous studies. <sup>13,26,34,35</sup> Figure 1(a) shows the morphology of the as-prepared  $\text{Li}_2\text{RuO}_3$ . The particle sizes are between 0.5 and 3  $\mu$ m, and the mean particle size is around 1.3  $\mu$ m. The HRTEM images are shown in Figure 1(b1) and (b2) which suggests that

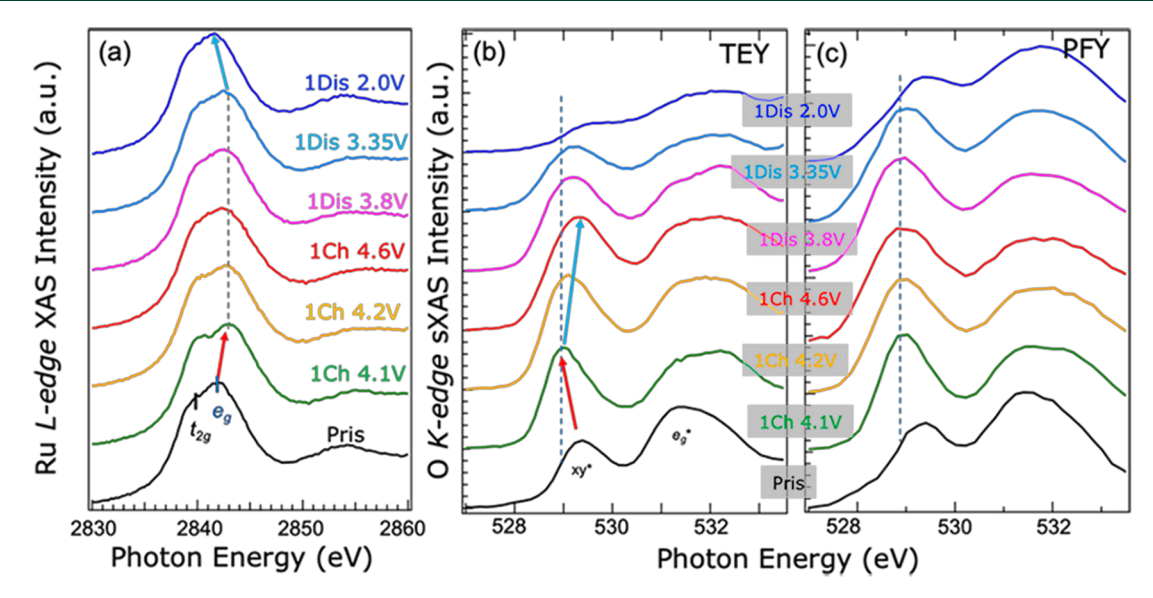


Figure 2. Ru state of Li<sub>2</sub>RuO<sub>3</sub> upon initial cycle. (a) The Ru-L<sub>3</sub> XAS spectra, (b) O-K TEY sXAS spectra, and (c) O-K PFY sXAS spectra of the Li<sub>2</sub>RuO<sub>3</sub> electrode at different electrochemical states which are marked as red dots in Figure 1(e) with Ch and Dis representing charge and discharge. The probe depth of Ru-L<sub>3</sub>, O-K TEY, and O-K PFY are several micrometres, 10 nm, and 150 nm, respectively.

the  ${\rm Li_2RuO_3}$  has a single crystalline structure. The synchrotron XRD in Figure 1(c) shows all diffraction peaks can be indexed in pdf 085-2000 (space group of C2/c) without obvious impurity phases. The extended cycles charge—discharge curves of  ${\rm Li_2RuO_3}$ , shown in Figure 1(d), are at a current density of 30 mA g $^{-1}$  between 2.0 and 4.6 V (vs  ${\rm Li/Li^+}$ ). The initial curve, with the first discharge capacities of 283 mAh g $^{-1}$ , is displayed in Figure 1(e) with 7 red dots indicating the samples characterized in the following spectroscopy measurements. There are two well-defined voltage plateaus upon the first cycle charge process, with the low-voltage one delivering around 170 mAh g $^{-1}$ . The cycling performance at a current density of 30 mA g $^{-1}$  is shown in Figure S1. The capacity decays quickly in the initial 10 cycles and then keeps relatively stable at around 220 mAh g $^{-1}$ . After 100 cycles, the capacity still remains at 180 mAh g $^{-1}$ .

The Ru- $L_3$  XAS collected on the electrode samples indicated by the red dots in Figure 1(e) are displayed in Figure 2(a). The Ru-L<sub>3</sub> XAS corresponds to excitations to directly the Ru 4d unoccupied orbitals, which indicates the Ru valence evolution. 16 The Ru- $L_3$  spectra consist of two features, which are assigned to the  $t_{2g}$  and  $e_g$  states due to spin-orbital splitting. It has been reported that the e<sub>g</sub> absorption peak is usually located at around 2842 eV for  $Ru^{4+}$  ( $Na_2RuO_3^{16}$  and  $SrRuO_3^{36}$ ) and 2843 eV for  $Ru^{5+}$  ( $NaRuO_3^{16}$  and  $Sr_4Ru_2O_9^{36}$ ). As shown in Figure 2(a), upon the low-voltage charge process (Pris to 1Ch4.1 V), the e<sub>o</sub> peak shifts to the high-energy position (red arrow) indicating the Ru valence varies from Ru<sup>4+</sup> to Ru<sup>5+</sup>, which is consistent with the low-voltage plateau of 170 mAh g<sup>-1</sup> capacity. Further charging at the high voltages (1Ch4.1 V to 1Ch4.6 V) does not lead to further variation of the e<sub>o</sub> absorption peak, suggesting no substantial change in the valence of Ru. During discharge, the e, peak of Ru remains unchanged before 3.35 V and shifts back to the original energy value at 2.0 V. Note the high photon energy of the Ru-L spectra leads to bulk sensitivity with a probe depth at the micrometer scale; therefore, the results show that bulk Ru redox reaction occurs at low-voltage range, below 4.1 V during charging and below 3.35 V during discharging.

The pre-edge of the O-K sXAS spectra collected on the same batch of samples in TEY (probe depth 10 nm) and PFY (probe

depth 150 nm) further provide the surface versus bulk Ru behaviors, as displayed in Figure 2(b) and 2(c), with the full energy range of TEY and TFY in Figure S2 and S3, respectively. The surface sensitive TEY signals (Figure S2) reveal a partially reversible surface carbonate (peaks at 534 eV) cycling in the early cycles, which resembles that on Li<sub>2</sub>MnO<sub>3</sub> surfaces but is not a focused topic of this study.<sup>32</sup> The O-K pre-edge features are dominated by hybridization orbitals of TM d and oxygen 2p with dominating Ru-4d characters.<sup>27,37</sup> Because higher TM oxidation states introduce lower energy O-K pre-edge features in oxide cathode materials, 27 the variations of the O-K XAS leading peak provides a probe of the Ru valence change upon cycling. For the relatively bulk-sensitive PFY, shown in Figure 2(c), the O-K pre-edge feature first shifts to the low-energy position, indicating the Ru valence oxidized from Ru<sup>4+</sup> to Ru<sup>5+</sup> at the 4.1 V charge state, and then it remains a steady charge to 4.6 V and discharge to 3.35 V. This is completely consistent with the Ru- $L_3$ results analyzed above, showing that the bulk Ru redox reaction occurs during the low-voltage charge process below 4.1 V and the discharge process below 3.35 V. For the surface-sensitive TEY XAS (Figure 2(b)), before the 4.1 V charge (1Ch4.1 V), the result is consistent with the PFY and Ru-L results, showing a shift of the leading peak toward the low-energy position, indicating the Ru oxidation. However, during the high-voltage charge process (1Ch4.1 V  $\rightarrow$  Ch4.2 V  $\rightarrow$  1Ch4.6 V), Figure 2(b) shows that pre-edge feature clearly shifts toward the highenergy position (blue arrow), indicating that the Ru is reduced on the surface during the high-voltage plateau. Such an opposite trend of surface Ru behavior is also observed during discharging, with a shift to low-energy position at 3.8 V and back to the highenergy value at 2.0 V discharge. These reversed behaviors of surface-sensitive spectra indicate a strong surface reaction at high voltages that affect Ru states, 10 which are often seen in other Li-rich compounds too. 32,38

To clarify the cycling mechanism of the high-voltage plateau that bulk Ru is inactive, we perform O-K mRIXS to detect the lattice ARR activities. Compared with conventional O-K XAS that is often dominated by TM characters, <sup>27</sup> O-K mRIXS has been established as a tool-of-choice for detecting the lattice ARR

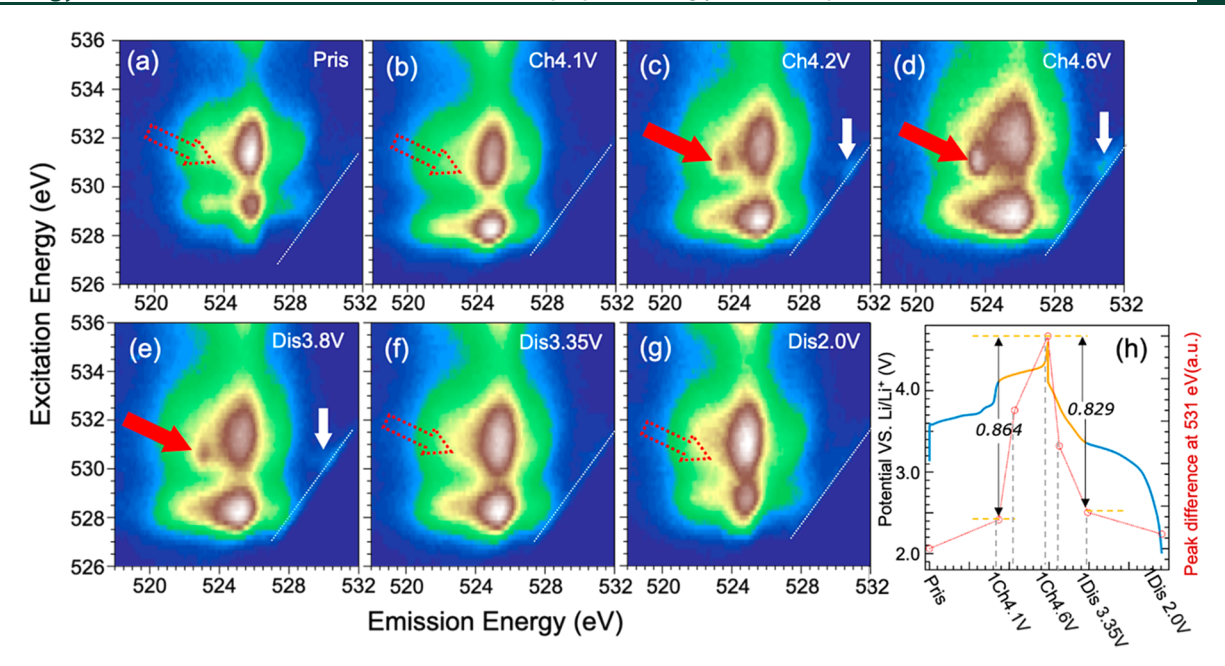


Figure 3. O-K mRIXS of a series of  $\text{Li}_2\text{RuO}_3$  electrodes at different electrochemical states. mRIXS images in (a)–(g) are collected from the electrodes indicated by the red dots on the electrochemical cycling profile in Figure 1(e). The solid red arrows indicated the striking sharp features of oxidized oxygen (anionic oxygen redox) at high-voltage state, e.g., Ch4.2 V, Ch4.6 V, and Dis3.8 V; in comparison, dotted red arrows are also marked at the same emission and excitation energy positions at the low-voltage state, e.g., Pris, Ch4.1 V, Dis3.35 V, and Dis2.0 V. White solid arrows display an energy loss feature, which is likely vibronic features accompanied by anionic oxygen redox. White dashed lines indicate the elastic lines, i.e., the line with the same excitation and emission energies. (h) is a summary of cationic Ru redox and the anionic O redox during the initial cycling profile. Colors of the profile lines represent roughly the different redox mechanism, blue for lattice Ru<sup>4+/5+</sup> and yellow for lattice oxygen redox. Hollow circles are the normalized areas of O-K mRIXS-sPFY (Figure S4) 531 eV peaks.

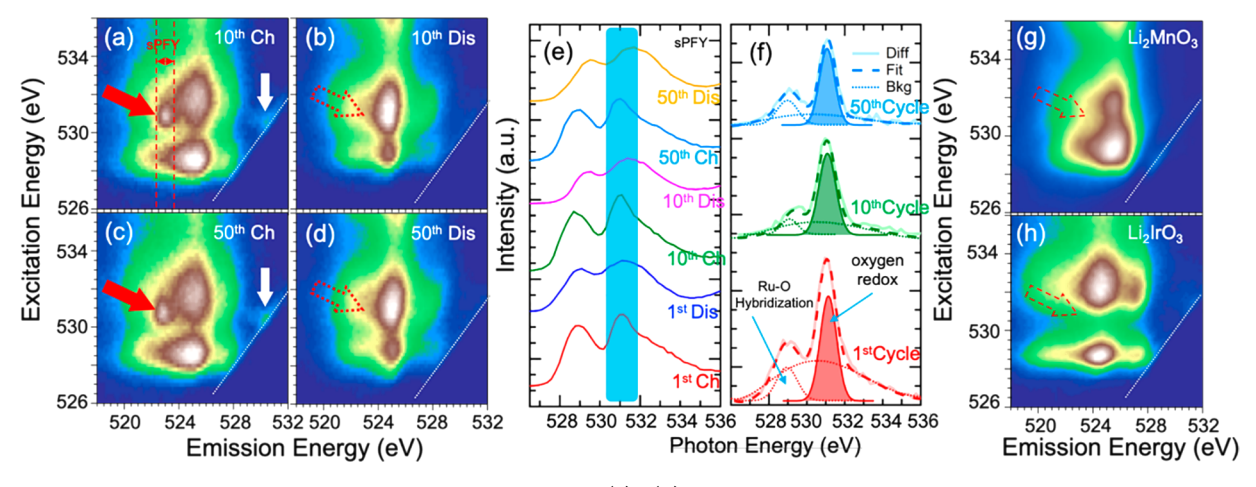


Figure 4. The cyclability analysis of  $\text{Li}_2\text{RuO}_3$ . O-K mRIXS images in (a)—(d) are collected from the electrodes upon 10th and 50th cycles. The solid red arrows indicated the anionic oxygen redox features at fully charged state. White solid arrows display an energy loss feature, which is likely vibronic features accompanied by anionic oxygen redox. Red dotted lines on mRIXS images indicate the energy range for extracting sPFY spectra. (e) shows the O-K mRIXS-sPFY spectra of extended cycles. The anionic oxygen redox contribution is reflected by the sPFY intensity difference within the shadow area between the charged and discharged state. (f) displays the difference between the sPFY spectra at charged and discharged locations. The solid and dashed lines represent the experimental spectral difference and fitted curves, respectively. The dotted lines are the polynomial background. The shaded Gaussian peaks under each spectrum represent the corresponding oxidized oxygen feature, with the other peak from Ru–O hybridization. (g) and (h) were collected from the 1st cycle fully charged electrodes of (g)  $\text{Li}_2\text{MnO}_3$ , reproduced from Zhuo et al.  $^{32}$  [Reprinted with permission from ref 32. Copyright 2021, Elsevier Inc.] and (h)  $\text{Li}_2\text{IrO}_3$ , reproduced from Hong et al.  $^{14}$  [Reprinted with permission from ref 14. Copyright 2019, Springer Nature].

states through its sensitivity to the intrinsically oxidized oxygen species.<sup>39,40</sup> Previous works have shown that characteristic mRIXS features around 531 eV excitation and 523.7 eV emission energies could be used to track the ARR activities in various battery cathodes.<sup>10,11,33,41,42</sup> Furthermore, a quantitative evaluation of the reversibility and cyclability of ARR reactions could

be gained through the mRIXS intensity variation upon electrochemical cycling. 10,11,33,41

Figure 3(a)-(g) display the O-K mRIXS images of the  $Li_2RuO_3$  electrodes at different states marked in Figure 1(e). Technical details of the mRIXS experiments are provided in the Supporting Information. The strong and broad features around

525.5 eV emission energy correspond to Ru-4d/O-2p hybridization states. These features get broadened in line shape and enhanced in intensity upon charging process, consistent with the XAS peak intensity increase (Figure 2(b)) but irrelevant to oxidized oxygen state. <sup>27,29</sup> At 4.2 V (Figure 3(c)), the mRIXS of  $\text{Li}_2\text{RuO}_3$  starts to display the fingerprint of oxidized O, indicated by the red arrow, with another low-energy excitation feature close to the elastic peak (white arrow). These oxidized oxygen features become stronger at the 4.6 V charge state (Figure 3(d)) and get weaker at the 3.8 V discharge state (Figure 3(e)) and disappear at discharge to 3.35 V (Figure 3(f)).

Figure 3(h) displays a summary of our Ru and O redox analysis with the normalized intensity of the O-K mRIXS oxidized oxygen feature (see the Supporting Information) plotted over the electrochemical profile. For ARR contributions, the O-K mRIXS-sPFY (in Figure S4) 531 eV peak intensity displays a changing ratio of 0.829/0.864 (96%) of the discharge/ charge process. Considering the surface reaction and gas release, 15 this spectral analysis ratio is more or less comparable with the electrochemical capacity of the ARR regimes. Consequently, the low-voltage charge plateau before 4.1 V with capacity 170 mAh/g is only compensated by Ru redox. For the high-voltage charge plateau above 4.1 V, the charge capacity of almost 120 mAh/g is related to the Li extraction from the lattice oxygen redox, accompanied by a strong surface reaction. For the following discharge slope above 3.35 V, the capacity 100 mAh/g comes mainly from the lattice oxygen redox. For the discharge below 3.35 V, the capacity 180 mAh/g is mainly coming from the Ru redox.

The intensity variation of the characteristic ARR mRIXS features could be used to tracks the reversibility and retention of the lattice ARR upon electrochemical cycling. 10,11,33,41 Figure 4(a)-(d) show O-K mRIXS of Li<sub>2</sub>RuO<sub>3</sub> electrodes at the 10th and 50th charged and discharged states. The oxidized oxygen feature remains strong after 10 and 50 cycles at the charged state and disappears upon discharging, indicating the reversible ARR after extended cycles. Integrating the intensity within the characteristic emission energy window around 523.7 eV (dashed lines in Figure 4(a)) yields the sPFY in Figure 4(e) at the first, 10th, and 50th cycles. The lines could be fitted by two Gaussian peaks in Figure 4(f), with the solid shaded peak corresponding to the lattice oxidized oxygen state as discussed above. Normalizing the peak intensity to the first cycle data, the peak intensities are 1, 0.803, and 0.768 for the first, 10th, and 50th cycle charged states, indicating 80% and 77% of the ARR capacity retention after 10 and 50 cycles, respectively.

For a direct comparison, Figure 4g and 4h display the mRIXS results of fully charged Li<sub>2</sub>MnO<sub>3</sub> and Li<sub>2</sub>IrO<sub>3</sub> reproduced from previous reports. 14,32 In sharp contrast, no feature of the ARR state in these charged electrodes could be observed. The Li<sub>2</sub>MnO<sub>3</sub> is a system with overactivated oxygen activities, leading to only irreversible oxidized oxygen through gas release and associated surface reactions, 32,44 with no lattice ARR found in any electrochemical stage.<sup>32</sup> As the other extreme case, Ir redox in Li<sub>2</sub>IrO<sub>3</sub> compensates for all the charge transfer upon charging through multivalent redox reactions, also leaving no ARR feature in mRIXS at the fully charged state as ARR is not activated until fully charged (Li  $\sim 0.5$ ). <sup>14</sup> In sharp contrast with Li<sub>2</sub>MnO<sub>3</sub> and Li<sub>2</sub>IrO<sub>3</sub>, O-K mRIXS Li<sub>2</sub>RuO<sub>3</sub> displays a strong and highly reversible ARR activity, with 96% initial cycle reversibility and 80%/77% capacity retention after 10/50 cycles, as analyzed above. Independent Ru-L and O-K characterizations show that the low- and high-voltage plateaus are separate from

the cationic and anionic redox reactions, although ARR is extended to much lower energy during the discharge. Therefore, the three  $\text{Li}_2\text{MO}_3$  systems behave distinctly on the oxygen activities, with a reversible ARR only in the LiRuO<sub>3</sub> system.

Clarifying the cycling mechanism and quantifying the highly reversible ARR in Li<sub>2</sub>RuO<sub>3</sub> triggers some interesting comparisons with the other Li<sub>2</sub>MO<sub>3</sub> systems. First, the strong and reversible ARR in Li<sub>2</sub>RuO<sub>3</sub> should not be taken for granted as a nature of the Li-rich configuration because the reaction is missing in both Mn and Ir systems. Instead, it indicates some other critical TM factors that are required to maintain a reversible lattice ARR. Second, compared with Li<sub>2</sub>IrO<sub>3</sub> with only Ir redox reactions, 13 Ru redox does take place; however, it cannot compensate for all the extraction of active Li. This is different from Li<sub>2</sub>IrO<sub>3</sub> and some other Li-rich compounds. For example, Li<sub>1.2</sub>Ni<sub>0.2</sub>Ru<sub>0.6</sub>O<sub>2</sub> does not involve ARR either, even at high voltages, due to the redox reactions of both Ni and Ru that could compensate all the cycling capacity. <sup>45</sup> Therefore, even for Li-rich compounds, the ARR is not necessarily enabled until the Li extraction content is higher than what the specific cationic redox reactions could compensate. This may sound simple and natural; however, it is important to note that the voltage range of the ARR remains an open question and is electrochemically (charge or discharge) dependent. The structural transformation, especially during the initial charging of Li-rich material, introduces a formidable challenge for theoretical simulations to reliably define the redox voltage range and its variation upon cycling. Therefore, the amount of available cationic redox reaction before ARR is highly material dependent. For example, some Na-poor compounds display clear signatures of ARR mixed with cationic redox even with a low capacity. 10 Third, compared with Li<sub>2</sub>MnO<sub>3</sub> that displays only irreversible oxygen oxidation,<sup>31</sup> the highly reversible ARR in Li<sub>2</sub>RuO<sub>3</sub> suggests another critical role of TMs in oxygen activities. 4d/5d TMs have been specifically emphasized in the ground-breaking works of the ARR concept due to their strong hybridization with O,13,46 which helps stabilize the ARR and improve its practicability. Indeed, replacing the Mn with Ru in the Li<sub>2</sub>MO<sub>3</sub> system largely suppresses the oxygen release, <sup>15,44,47</sup> and as clearly shown and quantified in this work, lattice ARR becomes strong and reversible in Li<sub>2</sub>RuO<sub>3</sub>.

Therefore, exhausting the available cationic redox determines whether oxygen will be oxidized during high-voltage charging. Once oxygen becomes electrochemically active, our comparison shows that the oxygen release and lattice ARR are two competing channels, and TM plays a critical role in determining the reaction route. The distinct oxygen activities in Li<sub>2</sub>MO<sub>3</sub> (M = Mn, Ru, Ir) strongly suggest the crucial role of the hybridization between TM and O for ARR, something emphasized earlier, 13,46 but got largely overlooked later due to the focus on nonbonding or unhybridized oxygen states. However, as emphasized in previous works,<sup>32</sup> it is equally important to note that the electron depopulation around O through the TM-O hybridization itself should not be considered a state of ARR, because all TM based cathode systems feature evolving hybridizations including LiFePO<sub>4</sub>. <sup>27</sup> The important question is how the hybridization between TM and O affects the ARR behavior so strongly, and how to reach the optimum TM-O hybridization. We expect this work will bring back the attention on the TM-O hybridization effect, instead of the overwhelming nonbonding state discussions, on ARR, and inspire further experimental and theoretical studies of TM oxides toward high-energy-density battery systems based on ARR.

## **■ EXPERIMENTAL METHODS**

Detailed descriptions of the experimental methods are shown in the Supporting Information

### ASSOCIATED CONTENT

# Supporting Information

The Supporting Information is available free of charge at https://pubs.acs.org/doi/10.1021/acsenergylett.1c01101.

Detailed synthesis and electrochemical testing process of Li<sub>2</sub>RuO<sub>3</sub>; full description of sample preparation for spectroscopy measurement; detailed technical information for spectroscopy measurement of both XAS and mRIXS; sPFY quantification process; additional electrochemical and spectroscopic data; figures of Capacity retention and Coulomb efficiency, XAS TEY and TFY, and sPFY(PDF)

# AUTHOR INFORMATION

#### **Corresponding Authors**

Gao Liu — Energy Storage and Distributed Resources Division, Energy Technologies Area, Lawrence Berkeley National Laboratory, Berkeley, California 94720, United States; orcid.org/0000-0001-6886-0507; Email: gliu@lbl.gov

Feng Pan — School of Advanced Materials, Peking University, Shenzhen Graduate School, Shenzhen 518055, China; oorcid.org/0000-0002-8216-1339; Email: panfeng@pkusz.edu.cn

Wanli Yang — Advanced Light Source, Lawrence Berkeley National Laboratory, Berkeley, California 94720, United States; orcid.org/0000-0003-0666-8063; Email: wlyang@lbl.gov

## **Authors**

Zengqing Zhuo — School of Advanced Materials, Peking University, Shenzhen Graduate School, Shenzhen 518055, China; Advanced Light Source, Lawrence Berkeley National Laboratory, Berkeley, California 94720, United States; orcid.org/0000-0001-6602-760X

Kehua Dai — College of Chemistry, Tianjin Normal University, Tianjin 300387, China; Advanced Light Source, Lawrence Berkeley National Laboratory, Berkeley, California 94720, United States

Jinpeng Wu — Advanced Light Source, Lawrence Berkeley National Laboratory, Berkeley, California 94720, United States; Stanford Institute for Materials and Energy Sciences, SLAC National Accelerator Laboratory, Menlo Park, California 94025, United States; Geballe Laboratory for Advanced Materials, Stanford University, Stanford, California 94305, United States; Department of Electrical Engineering, Tsinghua University, Beijing 100084, China

Liang Zhang — Advanced Light Source, Lawrence Berkeley National Laboratory, Berkeley, California 94720, United States; Occid.org/0000-0002-3446-3172

Nobumichi Tamura — Advanced Light Source, Lawrence Berkeley National Laboratory, Berkeley, California 94720, United States

Yi-de Chuang — Advanced Light Source, Lawrence Berkeley National Laboratory, Berkeley, California 94720, United States; orcid.org/0000-0002-2773-3840 Jun Feng – Department of Materials Science and Engineering, South University of Science and Technology, Shenzhen 518055, China

Jinghua Guo − Advanced Light Source, Lawrence Berkeley National Laboratory, Berkeley, California 94720, United States; © orcid.org/0000-0002-8576-2172

Zhi-xun Shen — Stanford Institute for Materials and Energy Sciences, SLAC National Accelerator Laboratory, Menlo Park, California 94025, United States; Geballe Laboratory for Advanced Materials, Stanford University, Stanford, California 94305, United States; Department of Physics and Applied Physics, Stanford University, Stanford, California 94305, United States

Complete contact information is available at: https://pubs.acs.org/10.1021/acsenergylett.1c01101

## **Author Contributions**

Zengqing Zhuo and Kehua Dai contributed equally to this work.

#### **Notes**

The authors declare no competing financial interest.

### ACKNOWLEDGMENTS

Synchrotron experiments were performed at the BL8.0.1.1 (RIXS), BL5.3.1 (XAS), and BL12.3.2 (SXRD) of the Advanced Light Source (ALS), a U.S. Department of Energy Office of Science User Facility. Material synthesis and structural characterizations were performed at the Energy Storage and Distributed Resources division, and the National Center for Electron Microscopy (NCEM), funded by the Assistant Secretary for Energy Efficiency, Vehicle Technologies Office of the U.S. Department of Energy. Z.Z. acknowledges the support of the Ph.D. student fellowship program of the ALS. All the Lawrence Berkeley National Laboratory efforts are under U.S. DOE contract no. DE-AC02-05CH11231. Works at Stanford are supported by the Department of Energy, Office of Science, Basic Energy Sciences, and Materials Sciences and Engineering Division, under contract no. DE-AC02-76SF00515.

## **■** REFERENCES

- (1) Armand, M.; Tarascon, J. M. Building better batteries. *Nature* **2008**, 451 (7179), 652–657.
- (2) Goodenough, J. B.; Kim, Y. Challenges for Rechargeable Li Batteries. *Chem. Mater.* **2010**, 22 (3), 587–603.
- (3) Assat, G.; Tarascon, J.-M. Fundamental understanding and practical challenges of anionic redox activity in Li-ion batteries. *Nat. Energy* **2018**, 3 (5), 373–386.
- (4) Xie, Y.; Saubanère, M.; Doublet, M. L. Requirements for reversible extra-capacity in Li-rich layered oxides for Li-ion batteries. *Energy Environ. Sci.* **2017**, *10* (1), 266–274.
- (5) Okubo, M.; Yamada, A. Molecular Orbital Principles of Oxygen-Redox Battery Electrodes. *ACS Appl. Mater. Interfaces* **2017**, 9 (42), 36463–36472.
- (6) Seo, D.-H.; Lee, J.; Urban, A.; Malik, R.; Kang, S.; Ceder, G. The structural and chemical origin of the oxygen redox activity in layered and cation-disordered Li-excess cathode materials. *Nat. Chem.* **2016**, 8 (7), 692–697.
- (7) Luo, K.; Roberts, M. R.; Hao, R.; Guerrini, N.; Pickup, D. M.; Liu, Y.-S.; Edström, K.; Guo, J.; Chadwick, A. V.; Duda, L. C.; Bruce, P. G. Charge-compensation in 3d-transition-metal-oxide intercalation cathodes through the generation of localized electron holes on oxygen. *Nat. Chem.* **2016**, 8 (7), 684–691.
- (8) McCalla, E.; Abakumov, A. M.; Saubanere, M.; Foix, D.; Berg, E. J.; Rousse, G.; Doublet, M. L.; Gonbeau, D.; Novak, P.; Van Tendeloo, G.;

- Dominko, R.; Tarascon, J. M. Visualization of O-O peroxo-like dimers in high-capacity layered oxides for Li-ion batteries. *Science* **2015**, *350* (6267), 1516–1521.
- (9) Rahman, M. M.; Lin, F. Oxygen Redox Chemistry in Rechargeable Li-Ion and Na-Ion Batteries. *Matter* **2021**, *4* (2), 490–527.
- (10) Wu, J.; Zhuo, Z.; Rong, X.; Dai, K.; Lebens-Higgins, Z.; Sallis, S.; Pan, F.; Piper, L. F. J.; Liu, G.; Chuang, Y.-d.; Hussain, Z.; Li, Q.; Zeng, R.; Shen, Z.-x.; Yang, W. Dissociate lattice oxygen redox reactions from capacity and voltage drops of battery electrodes. *Sci. Adv.* **2020**, *6* (6), No. eaaw3871.
- (11) Dai, K.; Mao, J.; Zhuo, Z.; Feng, Y.; Mao, W.; Ai, G.; Pan, F.; Chuang, Y.-d.; Liu, G.; Yang, W. Negligible voltage hysteresis with strong anionic redox in conventional battery electrode. *Nano Energy* **2020**, *74*, 104831.
- (12) Li, N.; Hwang, S.; Sun, M.; Fu, Y.; Battaglia, V. S.; Su, D.; Tong, W. Unraveling the Voltage Decay Phenomenon in Li-Rich Layered Oxide Cathode of No Oxygen Activity. *Adv. Energy Mater.* **2019**, 9 (47), 1902258.
- (13) Sathiya, M.; Rousse, G.; Ramesha, K.; Laisa, C. P.; Vezin, H.; Sougrati, M. T.; Doublet, M. L.; Foix, D.; Gonbeau, D.; Walker, W.; Prakash, A. S.; Ben Hassine, M.; Dupont, L.; Tarascon, J. M. Reversible anionic redox chemistry in high-capacity layered-oxide electrodes. *Nat. Mater.* **2013**, *12* (9), 827–835.
- (14) Hong, J.; Gent, W. E.; Xiao, P.; Lim, K.; Seo, D.-H.; Wu, J.; Csernica, P. M.; Takacs, C. J.; Nordlund, D.; Sun, C.-J.; Stone, K. H.; Passarello, D.; Yang, W.; Prendergast, D.; Ceder, G.; Toney, M. F.; Chueh, W. C. Metal—oxygen decoordination stabilizes anion redox in Li-rich oxides. *Nat. Mater.* **2019**, *18* (3), 256–265.
- (15) Ning, F.; Li, B.; Song, J.; Zuo, Y.; Shang, H.; Zhao, Z.; Yu, Z.; Chu, W.; Zhang, K.; Feng, G.; Wang, X.; Xia, D. Inhibition of oxygen dimerization by local symmetry tuning in Li-rich layered oxides for improved stability. *Nat. Commun.* **2020**, *11* (1), 4973.
- (16) Mortemard de Boisse, B.; Liu, G.; Ma, J.; Nishimura, S.-i.; Chung, S.-C.; Kiuchi, H.; Harada, Y.; Kikkawa, J.; Kobayashi, Y.; Okubo, M.; Yamada, A. Intermediate honeycomb ordering to trigger oxygen redox chemistry in layered battery electrode. *Nat. Commun.* **2016**, *7*, 11397.
- (17) Jimenez-Segura, M.-P.; Ikeda, A.; Kimber, S. A. J.; Giacobbe, C.; Yonezawa, S.; Maeno, Y. Effect of delithiation on the dimer transition of the honeycomb-lattice ruthenate Li2-xRuO3. *Phys. Rev. B: Condens. Matter Mater. Phys.* **2016**, *94* (11), 115163.
- (18) James, A. C. W. P.; Goodenough, J. B. Structure and bonding in lithium ruthenate, Li2RuO3. *J. Solid State Chem.* **1988**, 74 (2), 287–294.
- (19) Guerrini, N.; Jin, L.; Lozano, J. G.; Luo, K.; Sobkowiak, A.; Tsuruta, K.; Massel, F.; Duda, L.-C.; Roberts, M. R.; Bruce, P. G. Charging Mechanism of Li2MnO3. *Chem. Mater.* **2020**, 32 (9), 3733–3740.
- (20) Yang, Y.; Su, H.; Wu, T.; Jiang, Y.; Liu, D.; Yan, P.; Tian, H.; Yu, H. Atomic pair distribution function research on Li2MnO3 electrode structure evolution. *Sci. Bull.* **2019**, *64* (8), 553–561.
- (21) Boulineau, A.; Croguennec, L.; Delmas, C.; Weill, F. Structure of Li2MnO3 with different degrees of defects. *Solid State Ionics* **2010**, *180* (40), 1652–1659.
- (22) Boulineau, A.; Croguennec, L.; Delmas, C.; Weill, F. Reinvestigation of Li2MnO3 Structure: Electron Diffraction and High Resolution TEM. *Chem. Mater.* **2009**, *21* (18), 4216–4222.
- (23) Oishi, M.; Yamanaka, K.; Watanabe, I.; Shimoda, K.; Matsunaga, T.; Arai, H.; Ukyo, Y.; Uchimoto, Y.; Ogumi, Z.; Ohta, T. Direct observation of reversible oxygen anion redox reaction in Li-rich manganese oxide, Li2MnO3, studied by soft X-ray absorption spectroscopy. *J. Mater. Chem. A* **2016**, *4* (23), 9293–9302.
- (24) Han, S. J.; Xia, Y. G.; Wei, Z.; Qiu, B.; Pan, L. C.; Gu, Q. W.; Liu, Z. P.; Guo, Z. Y. A comparative study on the oxidation state of lattice oxygen among Li1.14Ni0.136Co0.136Mn0.544O2, Li2MnO3, Li-Ni0.5Co0.2Mn0.3O2 and LiCoO2 for the initial charge-discharge. *J. Mater. Chem. A* 2015, 3 (22), 11930–11939.
- (25) Yu, Y.; Karayaylali, P.; Nowak, S. H.; Giordano, L.; Gauthier, M.; Hong, W.; Kou, R.; Li, Q.; Vinson, J.; Kroll, T.; Sokaras, D.; Sun, C.-J.; Charles, N.; Maglia, F.; Jung, R.; Shao-Horn, Y. Revealing Electronic

- Signatures of Lattice Oxygen Redox in Lithium Ruthenates and Implications for High-Energy Li-Ion Battery Material Designs. *Chem. Mater.* **2019**, *31* (19), 7864–7876.
- (26) Mori, D.; Kobayashi, H.; Okumura, T.; Nitani, H.; Ogawa, M.; Inaguma, Y. XRD and XAFS study on structure and cation valence state of layered ruthenium oxide electrodes, Li2RuO3 and Li2Mn0.4-Ru0.6O3, upon electrochemical cycling. *Solid State Ionics* **2016**, 285, 66–74.
- (27) Roychoudhury, S.; Qiao, R.; Zhuo, Z.; Li, Q.; Lyu, Y.; Kim, J. H.; Liu, J.; Lee, E.; Polzin, B. J.; Guo, J.; Yan, S.; Hu, Y.; Li, H.; Prendergast, D.; Yang, W. Deciphering the Oxygen Absorption Pre-edge: A Caveat on its Application for Probing Oxygen Redox Reactions in Batteries. *Energy Environ. Mater.* **2021**, *4* (2), 246–254.
- (28) Lebens-Higgins, Z. W.; Chung, H.; Zuba, M. J.; Rana, J.; Li, Y.; Faenza, N. V.; Pereira, N.; McCloskey, B. D.; Rodolakis, F.; Yang, W.; Whittingham, M. S.; Amatucci, G. G.; Meng, Y. S.; Lee, T.-L.; Piper, L. F. J. How Bulk Sensitive is Hard X-ray Photoelectron Spectroscopy: Accounting for the Cathode–Electrolyte Interface when Addressing Oxygen Redox. *J. Phys. Chem. Lett.* **2020**, *11* (6), 2106–2112.
- (29) Yang, W.; Devereaux, T. P. Anionic and cationic redox and interfaces in batteries: Advances from soft X-ray absorption spectroscopy to resonant inelastic scattering. *J. Power Sources* **2018**, 389, 188–197
- (30) Wu, J.; Yang, Y.; Yang, W. Advances in soft X-ray RIXS for studying redox reaction states in batteries. *Dalton Trans* **2020**, 49, 13519–13527.
- (31) Rana, J.; Papp, J. K.; Lebens-Higgins, Z.; Zuba, M.; Kaufman, L. A.; Goel, A.; Schmuch, R.; Winter, M.; Whittingham, M. S.; Yang, W.; McCloskey, B. D.; Piper, L. F. J. Quantifying the Capacity Contributions during Activation of Li2MnO3. *ACS Energy Lett.* **2020**, *5*, 634–641.
- (32) Zhuo, Z.; Dai, K.; Qiao, R.; Wang, R.; Wu, J.; Liu, Y.; Peng, J.; Chen, L.; Chuang, Y.-d.; Pan, F.; Shen, Z.-x.; Liu, G.; Li, H.; Devereaux, T. P.; Yang, W. Cycling mechanism of Li2MnO3: Li—CO2 batteries and commonality on oxygen redox in cathode materials. *Joule* **2021**, *S* (4), 975–997.
- (33) Dai, K.; Wu, J.; Zhuo, Z.; Li, Q.; Sallis, S.; Mao, J.; Ai, G.; Sun, C.; Li, Z.; Gent, W. E.; Chueh, W. C.; Chuang, Y.-d.; Zeng, R.; Shen, Z.-x.; Pan, F.; Yan, S.; Piper, L. F. J.; Hussain, Z.; Liu, G.; Yang, W. High Reversibility of Lattice Oxygen Redox Quantified by Direct Bulk Probes of Both Anionic and Cationic Redox Reactions. *Joule* 2019, 3, 518.
- (34) Li, B.; Shao, R.; Yan, H.; An, L.; Zhang, B.; Wei, H.; Ma, J.; Xia, D.; Han, X. Understanding the Stability for Li-Rich Layered Oxide Li2RuO3 Cathode. *Adv. Funct. Mater.* **2016**, *26* (9), 1330–1337.
- (35) Sathiya, M.; Ramesha, K.; Rousse, G.; Foix, D.; Gonbeau, D.; Prakash, A. S.; Doublet, M. L.; Hemalatha, K.; Tarascon, J. M. High Performance Li2Ru1–yMnyO3 ( $0.2 \le y \le 0.8$ ) Cathode Materials for Rechargeable Lithium-Ion Batteries: Their Understanding. *Chem. Mater.* **2013**, 25 (7), 1121–1131.
- (36) Manoharan, S. S.; Sahu, R. K. Evidence for an anomalous redox ionic pair between Ru and Mn in SrRu0.5Mn0.5O3: An X-ray absorption spectroscopy approach. *Chem. Commun.* **2002**, 24, 3068–3069.
- (37) Frati, F.; Hunault, M. O. J. Y.; de Groot, F. M. F. Oxygen K-edge X-ray Absorption Spectra. *Chem. Rev.* **2020**, *120* (9), 4056–4110.
- (38) Zhang, J.; Wang, Q.; Li, S.; Jiang, Z.; Tan, S.; Wang, X.; Zhang, K.; Yuan, Q.; Lee, S. J.; Titus, C. J.; Irwin, K. D.; Nordlund, D.; Lee, J. S.; Pianetta, P.; Yu, X.; Xiao, X.; Yang, X. Q.; Hu, E.; Liu, Y. Depth-dependent valence stratification driven by oxygen redox in lithium-rich layered oxide. *Nat. Commun.* **2020**, *11* (1), 6342.
- (39) Zhuo, Z.; Pemmaraju, C. D.; Vinson, J.; Jia, C.; Moritz, B.; Lee, I.; Sallies, S.; Li, Q.; Wu, J.; Dai, K.; Chuang, Y.-d.; Hussain, Z.; Pan, F.; Devereaux, T. P.; Yang, W. Spectroscopic Signature of Oxidized Oxygen States in Peroxides. *J. Phys. Chem. Lett.* **2018**, 9 (21), 6378–6384.
- (40) Zhuo, Z.; Liu, Y.-S.; Guo, J.; Chuang, Y.-D.; Pan, F.; Yang, W. Full Energy Range Resonant Inelastic X-ray Scattering of O2 and CO2: Direct Comparison with Oxygen Redox State in Batteries. *J. Phys. Chem. Lett.* **2020**, *11* (7), 2618–2623.

- (41) Lee, G.-H.; Wu, J.; Kim, D.; Cho, K.; Cho, M.; Yang, W.; Kang, Y.-M. Reversible Anionic Redox Activities in Conventional LiNi1/3Co1/3Mn1/3O2 Cathodes. *Angew. Chem.* **2020**, *132* (22), 8759–8766
- (42) Li, Q.; Lebens-Higgins, Z. W.; Li, Y.; Meng, Y. S.; Chuang, Y. D.; Piper, L. F. J.; Liu, Z.; Yang, W. Could Irradiation Introduce Oxidized Oxygen Signals in Resonant Inelastic X-ray Scattering of Battery Electrodes? *J. Phys. Chem. Lett.* **2021**, *12*, 1138–1143.
- (43) Wu, J.; Li, Q.; Sallis, S.; Zhuo, Z.; Gent, W. E.; Chueh, W. C.; Yan, S.; Chuang, Y.-d.; Yang, W. Fingerprint Oxygen Redox Reactions in Batteries through High-Efficiency Mapping of Resonant Inelastic X-ray Scattering. *Condens Matter* **2019**, *4* (1), 5.
- (44) Rana, J.; Papp, J. K.; Lebens-Higgins, Z.; Zuba, M.; Kaufman, L. A.; Goel, A.; Schmuch, R.; Winter, M.; Whittingham, M. S.; Yang, W.; McCloskey, B. D.; Piper, L. F. J. Quantifying the Capacity Contributions during Activation of Li2MnO3. *ACS Energy Lett.* **2020**, 5 (2), 634–641.
- (45) Xu, J.; Sun, M.; Qiao, R.; Renfrew, S. E.; Ma, L.; Wu, T.; Hwang, S.; Nordlund, D.; Su, D.; Amine, K.; Lu, J.; McCloskey, B. D.; Yang, W.; Tong, W. Elucidating anionic oxygen activity in lithium-rich layered oxides. *Nat. Commun.* **2018**, *9* (1), 947.
- (46) Grimaud, A.; Hong, W. T.; Shao-Horn, Y.; Tarascon, J. M. Anionic redox processes for electrochemical devices. *Nat. Mater.* **2016**, 15 (2), 121–6.
- (47) Ramakrishnan, S.; Park, B.; Wu, J.; Yang, W.; McCloskey, B. D. Extended Interfacial Stability through Simple Acid Rinsing in a Li-Rich Oxide Cathode Material. *J. Am. Chem. Soc.* **2020**, *142* (18), 8522–8531.